Nano Research 2016, 9(5): 1300–1309
DOI 10.1007/s12274-016-1025-x
Research Article
ISSN 1998-0124
CN 11-5974/O4

Nanowires assembled from $MnCo_2O_4$@C nanoparticles for water splitting and all-solid-state supercapacitor

Chencheng Sun[1], Jun Yang[1], Ziyang Dai[1], Xuewan Wang[2], Yufei Zhang[1], Laiquan Li[1], Peng Chen[2] (✉), Wei Huang[1] (✉), and Xiaochen Dong[1] (✉)

[1] *Key Laboratory of Flexible Electronics (KLOFE) & Institute of Advanced Materials (IAM), Jiangsu National Synergetic Innovation Center for Advanced Materials (SICAM), Nanjing Tech University (NanjingTech), 30 South Puzhu Road, Nanjing 211816, China*
[2] *School of Chemical and Biomedical Engineering, Nanyang Technological University, 62 Nanyang Drive, 637459, Singapore*

Received: 8 December 2015
Revised: 17 January 2016
Accepted: 20 January 2016

KEYWORDS
transition metal oxide, nitrogen doped carbon, oxygen evolution, supercapacitor

ABSTRACT

The rational design of earth-abundant catalysts with excellent water splitting activities is important to obtain clean fuels for sustainable energy devices. In this study, mixed transition metal oxide nanoparticles encapsulated in nitrogen-doped carbon (denoted as AB_2O_4@NC) were developed using a one-pot protocol, wherein a metal–organic complex was adopted as the precursor. As a proof of concept, $MnCo_2O_4$@NC was used as an electrocatalyst for water oxidation, and demonstrated an outstanding electrocatalytic activity with low overpotential to achieve a current density of 10 mA·cm^{-1} (η_{10} = 287 mV), small Tafel slope (55 mV·dec^{-1}), and high stability (96% retention after 20 h). The excellent electrochemical performance benefited from the synergistic effects of the $MnCo_2O_4$ nanoparticles and nitrogen-doped carbon, as well as the assembled mesoporous nanowire structure. Finally, a highly stable all-solid-state supercapacitor based on $MnCo_2O_4$@NC was demonstrated (1.5% decay after 10,000 cycles).

1 Introduction

The increasingly serious global energy and environmental problems have speeded up the research on clean and sustainable energy storage and conversion systems [1–3]. The electrochemical splitting of water to hydrogen and/or oxygen is one the most promising approaches to generate clean fuels from renewable energy sources [4, 5]. However, the water splitting efficiency is usually limited by the oxygen evolution reaction (OER) at the anode because of the high overpotential and poor reversibility [6, 7]. In addition, the currently used noble catalysts (e.g., IrO_2 and RuO_2) always suffer from high cost and poor durability [8, 9]. Therefore, many efforts have been made to design superior electrocatalysts for water oxidation [10–12].

Mixed-valence transition metal oxides (MTMOs), typically with a spinel structure, are promising electrode materials for OER because of their improved conductivity and greater number of valence states compared

Address correspondence to Xiaochen Dong, iamxcdong@njupt.edu.cn; Wei Huang, iamwhuang@njtech.edu.cn; Peng Chen, chenpeng@ntu.edu.sg

to single metal oxides [13, 14]. Moreover, their catalytic and electrochemical properties can be easily tuned by adjusting the ratio of the metal element [15]. However, their practical application is prevented by their insufficient conductivity and stability [16, 17]. Nitrogen-doped (N-doped) carbon materials (e.g., N-doped carbon nanotubes [18], N-doped carbon foam [19], and N-doped graphene [20, 21]) also exhibit good OER catalyst properties as a result of the introduction of electron-rich dopants without a lattice mismatch [22–24]. Although the catalytic activity of N-doped carbon materials is less than that of MTMOs, they are highly stable. Hence, the hybridization N-doped carbon and MTMO nanoparticles may lead to synergistic effects that could improve their catalytic performance in water splitting [25, 26]. For example, Qiao et al. synthesized a three-dimensional electrode by hybridizing $NiCo_2O_4$ and N-doped graphene, which showed an OER catalytic performance comparable to noble metal catalysts both in kinetics and in stability [27]. Although much effort have been made to synthesize various MTMO-based composites, the rational design and facile synthesis of MTMO nanoparticles well confined in N-doped porous carbon is still a huge challenge [28].

This study demonstrated a simple synthetic route to produce mesoporous nanowires assembled from MTMO nanoparticles encapsulated by N-doped carbon ($MnCo_2O_4$@NC, $NiMn_2O_4$@NC, or $NiCo_2O_4$@NC). As a proof, when used as an anode, the $MnCo_2O_4$@NC exhibited superior catalytic activity and improved durability in comparison to those of a commercial RuO_2 catalyst. Furthermore, a highly stable all-solid-state supercapacitor based on $MnCo_2O_4$@NC was demonstrated.

2 Materials and experimental section

2.1 Synthesis of $MnCo_2O_4$@NC nanowires

All of the chemical regents were of analytical grade and directly used as received without any purification. Consider the synthesis of $MnCo_2O_4$@NC as an example. First, 3.0 mmol of $MnCl_2{\cdot}4H_2O$, 6.0 mmol of $CoCl_2{\cdot}6H_2O$, and 0.9 g of nitrilotriacetic acid (NA) were added to a mixed solvent containing 30.0 mL of isopropyl alcohol and 10.0 mL of deionized water with vigorous stirring until complete dissolution. Then, the mixture was transferred into a Teflon-lined autoclave, which was heated to 180 ℃ and maintained for 6 h. A pink product was collected by centrifugation and washed several times with deionized water and ethanol, resulting in the so-called $MnCo_2$-NA. The $MnCo_2$-NA powder was placed in a tube furnace and heated to 450 ℃ for 1 h with a ramp of 2 ℃·min^{-1} under an argon gas flow. Finally, the product was removed, and a color change from pink to black was observed. For comparison, $MnCo_2O_4$ nanoparticles without the encapsulation of carbon were obtained by directly calcinating the $MnCo_2$-NA under identical experimental conditions, except the gas flow was changed to one of air.

As for the $NiCo_2O_4$@NC and $NiMn_2O_4$@NC, their syntheses were similar to that of $MnCo_2O_4$@NC, except the metal salts were replaced by corresponding ones (3.0 mmol $NiCl_2{\cdot}6H_2O$ and 6.0 mmol $CoCl_2{\cdot}6H_2O$ for $NiCo_2O_4$@NC, and 3.0 mmol $NiCl_2{\cdot}6H_2O$ and 6.0 mmol $MnCl_2{\cdot}4H_2O$ for $NiMn_2O_4$@NC).

2.2 Material characterization

The phase purity of all the products was characterized using an X-ray powder diffractometer (Bruker D8 Advance) with Cu Kα radiation (λ = 1.5406 Å). The morphology and nanostructure of each product were examined using field-emission scanning electron microscopy (FESEM, JEOL JSM-7600F) and transmission electron microscopy (TEM, JEOL JSM-2100F), respectively. An energy dispersive X-ray (EDX) analysis and elemental mapping were conducted using the X-ray spectroscope attached to the JEM-2100F. The chemical compositions of the samples were analyzed using X-ray photoelectron spectroscopy (XPS) (Axis Ultra (Kratos Analytical, UK) with an Al Kα source (1,486.6 eV). Thermogravimetric analysis (TGA) measurements were performed on a Shimadzu-60 thermoanalyzer with a temperature ramp of 2 ℃·min^{-1} under an argon atmosphere. Raman spectroscopy was performed with a micro-Raman system (Renishaw InVia) using a laser excitation wavelength of 514 nm. The BET specific surface areas and corresponding pore distributions of the samples were examined based on the nitrogen adsorption/desorption at 77 K (Autosorb AS-6B).

2.3 Electrocatalytic OER test

The OER activities of the catalysts were measured in a standard three-electrode glass cell filled with 0.1 mol·L^{-1} (M) KOH electrolyte on a CH Instruments 760D electrochemical workstation. Glassy carbon electrodes (5 mm in diameter) with various catalysts were employed as the working electrode, and a Pt wire and Ag/AgCl electrode were used for the counter and reference electrodes, respectively. For the fabrication of the working electrode, 5.0 mg of the synthesized catalyst was dispersed in a mixed solution composed of 100 μL of a Nafion solution (5.0% Nafion in ethanol) and 900 μL of deionized water by sonication. Then, 10.0 μL of the suspension was dropped onto a glassy carbon electrode to provide a mass loading of 0.2 mg·cm^{-2}, and the electrode was naturally dried overnight. O_2 saturation was maintained during the collection of data in order to ensure the O_2/H_2O equilibrium at 1.23 V vs. the reversible hydrogen electrode (RHE) potential. Linear sweep voltammetry was carried out from 0 to 1.0 V (vs. Ag/AgCl) at 5 mV·s^{-1} for the polarization curves. The catalyst was cycled dozens of times using cyclic voltammetry (CV) until a stable CV curve was obtained before testing. The electrode potential reported in this work is relative to the RHE potential, which was converted from the Ag/AgCl electrode using $E_{RHE} = E_{(Ag/AgCl)} + 0.96$ V.

The stability was tested in an O_2-saturated 0.1 M KOH solution at a sweep rate of 100 mV·s^{-1} for 4,000 cycles at 1.2–1.6 V vs. RHE. Then, the resulting electrode was used to obtain polarization curves at a sweep rate of 5 mV·s^{-1}.

2.4 Characterization of all-solid-state supercapacitor (ASC)

ASC devices were fabricated according to Ref. [29]. First, a polyethylene terephthalate (PET) substrate was coated with Ag electrodes using a screen printer and dried at 200 ℃ in a vacuum oven. Subsequently, the $MnCo_2O_4$@NC solution was printed on the top of the Ag electrodes and dried at 110 ℃ in a vacuum oven (the mass loading of $MnCo_2O_4$@NC was around 4.0 mg·cm^{-2}). Finally, a PVA/KOH electrolyte was spread on the top of the device to cover the channel area. The electrochemical performance of the ASC was measured using an electrochemical workstation (VMP3, Biologic). The CV and galvanostatic charge/discharge were studied at various scan rates and current densities. Electrochemical impedance spectroscopy (EIS) was carried out with frequencies of 100 kHz to 0.1 Hz using a sinusoidal signal with an amplitude of 5 mV.

3 Results and discussion

As schematically illustrated in Fig. 1, the NA molecules could react with two different transition metal ions via carboxyl groups and polymerized into nanowires under hydrothermal conditions. Three peaks at 1,676, 1,648, and 1,578 cm^{-1}, corresponding to the bonding between the metal ions (Mn^{2+} or Co^{2+}) and carboxylate groups on NA, could be observed from the Fourier transform infrared spectroscopy (FTIR, Fig. S1(a) in the Electronic Supplementary Material (ESM)) spectra, indicating the formation of $MnCo_2$-NA. FESEM and TEM images revealed that the length of the resulting $MnCo_2$-NA nanowires was several micrometers, with a uniform diameter (~50 nm) (Figs. S1(b)–S1(d) in the ESM).

The TGA curve in Fig. S2 in the ESM shows that there was little weight loss for the $MnCo_2$-NA at temperatures higher than 400 ℃, indicating that the $MnCo_2O_4$@NC hybrid could be obtained by calcinating $MnCo_2$-NA in an argon atmosphere at 450 ℃. As shown in Fig. 2(a), the $MnCo_2O_4$@NC preserved the nanowire morphology of the precursor, except the surface became rough. TEM images reveal that the $MnCo_2O_4$@NC nanowires were composed of numerous nanoparticles

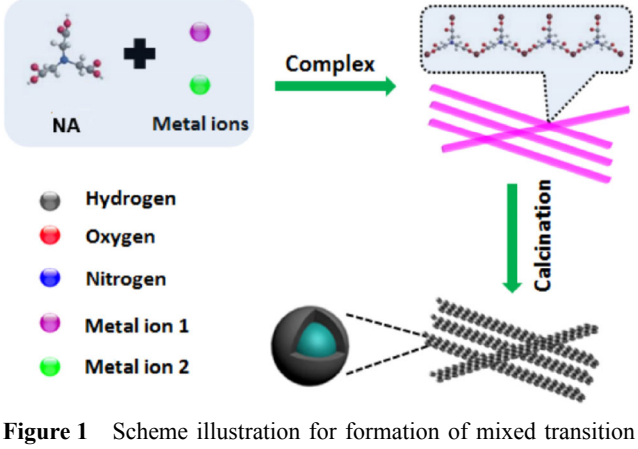

Figure 1 Scheme illustration for formation of mixed transition metal oxide nanoparticles encapsulated in nitrogen-doped carbon.

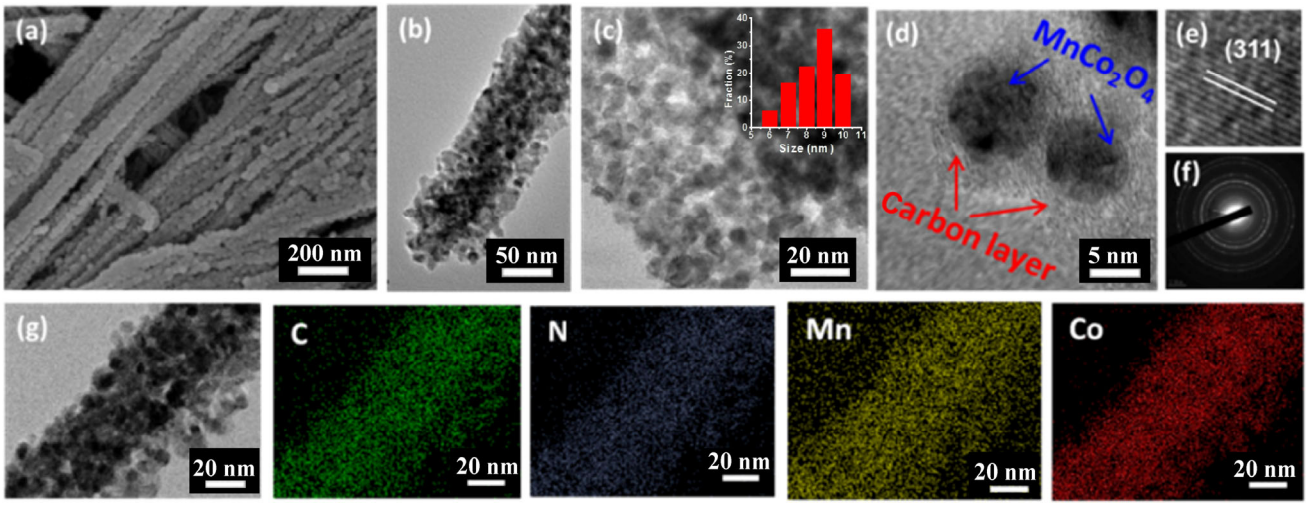

Figure 2 (a) FESEM, (b) and (c) TEM images of $MnCo_2O_4$@NC (inset in (c) shows size distribution of $MnCo_2O_4$). (d) and (e) HRTEM images of $MnCo_2O_4$@NC. (f) SEAD image of $MnCo_2O_4$@NC. (g) TEM and elemental mapping images showing the homogenous distribution of C, N, Mn, and Co in $MnCo_2O_4$@NC.

with a diameter of approximately 50 nm (Fig. 2(b)). A magnified TEM image shows that the $MnCo_2O_4$@NC nanoparticles were well-dispersed, with an average diameter of less than 10 nm (Fig. 2(c)). A high-resolution TEM (HRTEM) image indicates that the $MnCo_2O_4$ nanoparticles are completely encapsulated by a carbon layer and form a core–shell structure (Fig. 2(d)). The thickness of the carbon layer is about 2 nm. In contrast, the $MnCo_2O_4$ nanowires are composed of large nanoparticles with a size greater than 100 nm (Fig. S3 in the ESM). These results demonstrate that the carbon layer could restrict the growth of the $MnCo_2O_4$ nanoparticles and ensure a uniform distribution. Figure 2(e) shows that the interplane spacing of the $MnCo_2O_4$ is 0.25 nm, which corresponds very well to the (311) plane of tetragonal $MnCo_2O_4$. In addition, the electron diffraction ring patterns suggest that the $MnCo_2O_4$ has a polycrystalline structure (Fig. 2(f)). Elemental mapping demonstrated the uniform distribution of the Mn, Co, N, and C elements in the $MnCo_2O_4$@NC nanowire (Fig. 2(g)). An energy-dispersive spectroscopy (EDS) measurement (Fig. S4 in the ESM) demonstrated that the atomic ratio of the Mn:Co:O in the hybrid was 11.5:24.2:43.3, which was close to the stoichiometry of $MnCo_2O_4$. Based on the EDS result, the $MnCo_2O_4$ content in the hybrid could be calculated to be approximately 90 wt.%, which indicated high-loading transition metal oxide nanoparticles encapsulated in N-doped carbon.

Figure 3(a) shows the X-ray diffraction (XRD) pattern of $MnCo_2O_4$@NC. All of the diffraction peaks closely match the JCPDS data (card No. 23-1237), except the peak located at 26°, which could indicate the existence of carbon [30]. In the Raman spectra (Fig. 3(b)), two prominent peaks at 1,350 and 1,598 cm^{-1} correspond to the D and G modes of carbon, respectively [31]. The additional characteristic peak at 690 cm^{-1}, corresponding to the stretching vibration mode of M–O (M = Mn, Co), further confirms the integration of $MnCo_2O_4$ with a N-doped carbon shell [32]. It is widely accepted that the formation of C–O–metal or C–N– metal bonds between N-doped carbon and spinel oxide nanoparticles can increase the activity of the catalytic sites in the hybrid [5, 33, 34]. Figure 3(c) shows the XPS spectrum for $MnCo_2O_4$@NC. The defined peaks for the Mn, Co, O, N, and C elements can be clearly observed. In addition, the high-resolution N 1s spectrum can be deconvoluted into three types of N species corresponding to pyridinic N (398.0 eV, 34 at.%), pyrrolic N (399.3 eV, 17 at.%), and graphitic N (400.5 eV, 49 at.%) (Fig. 3(d)) [35]. The incorporation of various nitrogen species can change the density of state and decrease the local surface function of graphitic carbon, and enhance the electrochemical performance for OER [36–38]. Based on the N_2 adsorption–desorption measurement, the $MnCo_2O_4$@NC nanowires could be

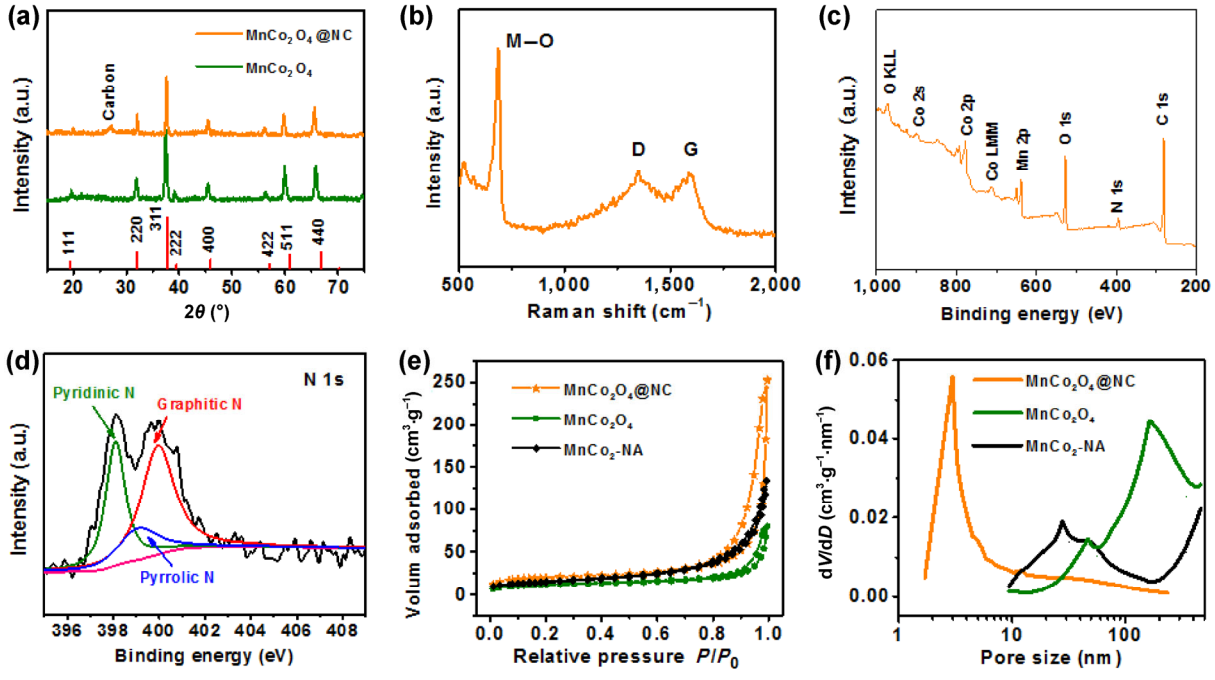

Figure 3 (a) XRD patterns of $MnCo_2O_4$@NC and $MnCo_2O_4$. (b) Raman spectrum of $MnCo_2O_4$@NC. (c) and (d) XPS spectra and high resolution N 1s spectrum of $MnCo_2O_4$@NC. (e) and (f) N_2 adsorption/desorption isotherms and corresponding pore size distributions of $MnCo_2O_4$@NC, $MnCo_2O_4$, and $MnCo_2$-NA.

calculated to display a large specific surface area of 153.2 $m^2 \cdot g^{-1}$, which outperformed $MnCo_2$-NA (42.8 $m^2 \cdot g^{-1}$) and $MnCo_2O_4$ (38.5 $m^2 \cdot g^{-1}$) (Fig. 3(e)). In addition, the presence of a hysteresis loop at relative pressures of 0.8–1.0 demonstrated that the $MnCo_2O_4$@NC nanowires had a mesoporous structure with a pore diameter of approximately 3 nm (Fig. 3(f)) [39].

$MnCo_2O_4$@NC hybrid films of the samples were prepared on glassy carbon electrodes with a mass loading of 0.2 mg·cm^{-2} for linear sweep voltammetry (LSV) in 0.1 M KOH using a standard three-electrode setup, as described in the experimental section. Figure 4(a) shows the polarization curves obtained from the $MnCo_2O_4$@NC nanowires. Compared with the single $MnCo_2O_4$, a much earlier OER onset potential could be observed (Table 1). The OER activity was also compared using the required overpotentials to achieve a current density of 10 mA·cm^{-2} (η_{10}). For $MnCo_2O_4$@NC, the η_{10} was 287 mV, which was greatly improved compared with $MnCo_2O_4$ and even lower than that of the commercial RuO_2 catalyst (η_{10} = 325 mV). The OER kinetics of $NiCo_2O_4$@NC were estimated using Tafel plots, and the linear region was fitted via the Tafel equation: $\eta = b \times \log j + a$ (where η is the overpotential, j is the current density, and b is the Tafel slope). From Fig. 4(b), the calculated Tafel slope of $MnCo_2O_4$@NC is about 55 mV·dec^{-1}, which is superior to that of commercial RuO_2 (69 mV·dec^{-1}) and $MnCo_2O_4$ (101 mV·dec^{-1}). This indicated that the favorable OER kinetics of $MnCo_2O_4$@NC and the second electron transfer were the main rate-determining step [40]. Furthermore, compared with the reported MTMO-based electrodes, $MnCo_2O_4$@NC exhibited a high catalytic activity toward the OER in both the onset potential and Tafel slope (Table S1 in the ESM).

Such a remarkable electrocatalytic performance of $MnCo_2O_4$@NC could be attributed to the synergistic effects of the ultrasmall $MnCo_2O_4$ particles, carbon layer, and nitrogen doping, as well as the unique structure. First, the small (less than 10 nm) $MnCo_2O_4$ particles could offer abundant active sites to promote rapid oxygen adsorption and desorption in an alkaline electrolyte. Second, the carbon layer could not only increase the electrochemical conductivity and surface area, but also prevent $MnCo_2O_4$ nanoparticles from aggregating and provide more exposed active sites [41, 42]. Third, a nitrogen source derived from an amino

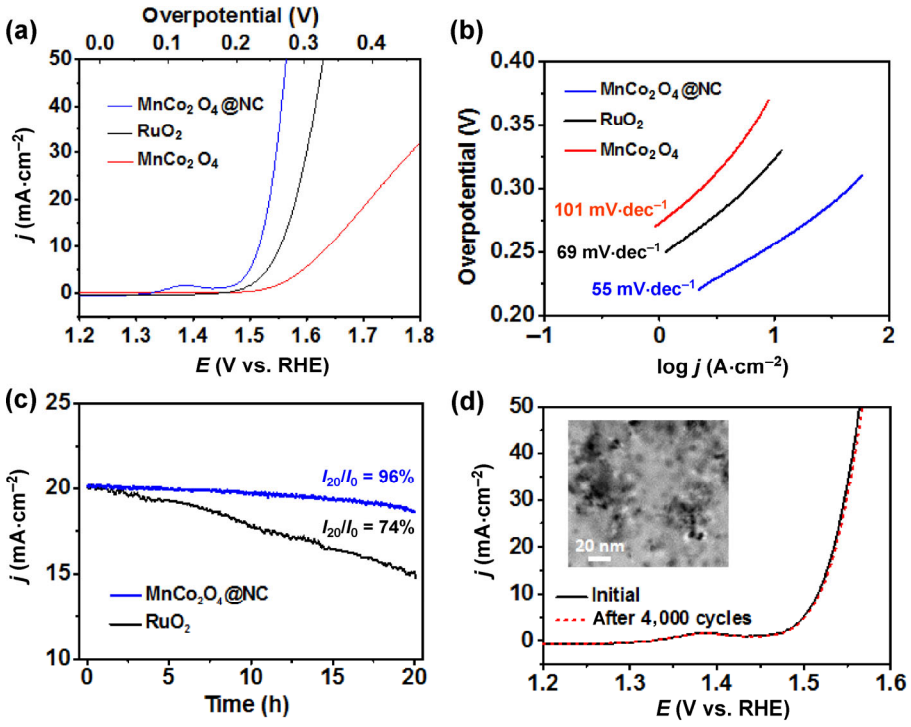

Figure 4 (a) Polarization curves and (b) corresponding Tafel plots of $MnCo_2O_4$@NC, $MnCo_2O_4$, and RuO_2 at 5 mV·s^{-1}. (c) Stability of $MnCo_2O_4$@NC and RuO_2 at a current density of 20 mA·cm^{-2}. (d) Polarization curves of $MnCo_2O_4$@NC before and after 4,000 potential cycles (scan rate 5 mV·s^{-1}). Inset shows TEM image of $MnCo_2O_4$@NC after 4,000 cycles.

Table 1 OER activity of $MnCo_2O_4$@NC, $MnCo_2O_4$, and RuO_2

Catalyst	Onset potential (V vs. RHE)	η@ j = 10 mA·cm^{-2} (mV)	Tafel slope (mV·dec^{-1})
$MnCo_2O_4$@NC	1.459	287	55
RuO_2	1.482	325	69
$MnCo_2O_4$	1.531	411	101

group in the organic linker played an indispensable role in the OER performance. In addition, the unique nanoparticle-assembled porous structure allowed the exposed active sites to easily contact the electrolyte.

The durability of $MnCo_2O_4$@NC was assessed using chronoamperometry and voltammetric cycling measurements over 4,000 cycles. As shown in Fig. 4(c), the current density of $MnCo_2O_4$@NC could be maintained at 20 mA·cm^{-2} with a decay of only 4% over 20 h of operation, which was superior to that of the commercial RuO_2 catalyst (26%, η = 321 mV). In addition, the negligible change in the *I*–*V* curves after 4,000 cycles further confirmed the excellent cycling stability of $MnCo_2O_4$@NC (Fig. 4(d)). The excellent stability of $MnCo_2O_4$@NC also came from its unique core–shell structure. Here, N-doping carbon shells could effectively immobilize the uniformly distributed $MnCo_2O_4$ nanoparticles and prevent their aggregation (inset in Fig. 4(d)). The conductivity of MTMO could also be remarkably improved by hybridization with carbon materials [43].

MTMO/carbon is also well known as an active electrode material for supercapacitors [44]. When used as an electrode material, the typical CV curves of a $MnCo_2O_4$@NC-based ASC measured at different scan rates are shown in Fig. 5(a). Their quasi-rectangular shapes indicate that the ASC presents an electrical double layer capacitor (EDLC)-like capacitive behavior. On the other hand, the well-preserved shapes from 5 to 100 mV·s^{-1} suggest the high rate capability of

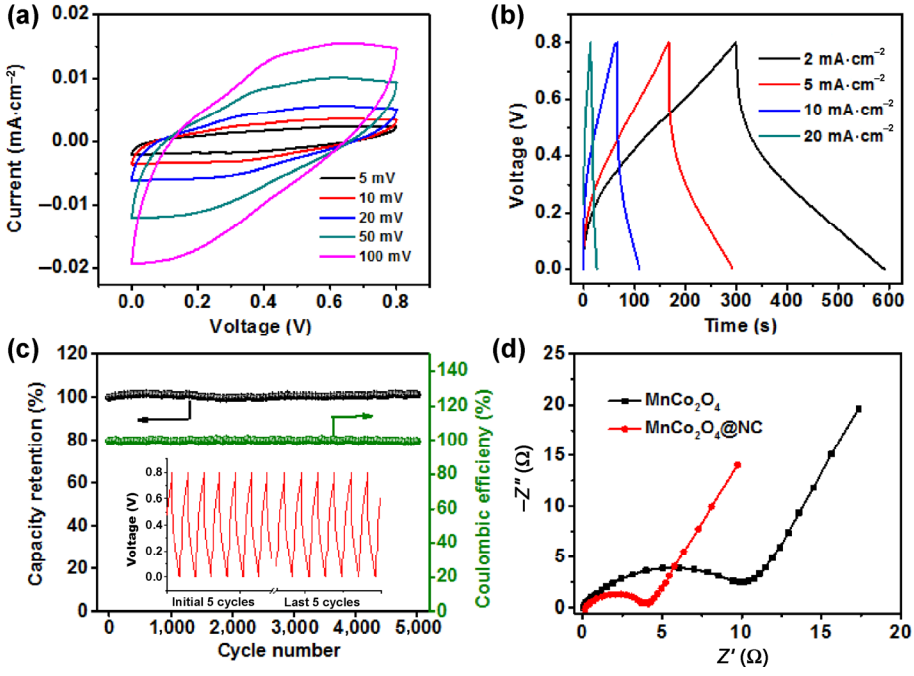

Figure 5 (a) CV curves of $MnCo_2O_4$@NC ASC at various scan rates. (b) Galvanostatic charge/discharge curves at various current densities. (c) Cycling stability of $MnCo_2O_4$@NC ASC at a current density of 20 mA·cm^{-2}. Inset is the profile of initial and last five charge/discharge cycles. (d) Nyquist plots of $MnCo_2O_4$ and $MnCo_2O_4$@NC.

$MnCo_2O_4$@NC for power delivery [45]. The symmetric galvanostatic charge/discharge curves of the $MnCo_2O_4$@NC ASC obtained at various current densities indicate its superior capacitive behavior. Figure S5 in the ESM shows the relationship between the areal specific capacitance and the current density. At a current density of 20 μA·cm^{-2}, its specific capacitance could reach 846 mF·cm^{-2}. With an increase in the current density to 20 mA·cm^{-2}, a high capacitance of 683 mF·cm^{-2} still remained, which was superior to those of many reported MTMO/carbon composites [46–49]. Figure 5(c) shows the cyclic stability of the ACS at a current density of 20 mA·cm^{-2}. It indicates that the capacity retention of the ACS remained at 98.5% after 10,000 charge/discharge cycles. Moreover, the shapes of the CV curves were not significantly changed before and after the long-term process, as shown in the inset of Fig. 5(c). The remarkable long-term stability of the electrode arose from the unique NC-encapsulated $MnCo_2O_4$ structure, which allowed a large strain accommodation in the charge/discharge process [50–53]. Electrochemical impedance spectroscopy was conducted to explore the kinetic properties of the $MnCo_2O_4$@NC and $MnCo_2O_4$. Both plots in Fig. 5(d) show a semicircle associated with the charge transfer resistance at higher frequencies, followed by a sloped line ascribed to the diffusion resistance at lower frequencies. It can be seen that $MnCo_2O_4$@NC and $MnCo_2O_4$ exhibit similar diffusion resistances. However, the charge transfer resistance of $MnCo_2O_4$@NC is much smaller, indicating that the NC coverage could significantly boost the electronic conductivity and enable much easier charge transfer at the electrode/electrolyte interface.

More importantly, our protocol could be further extended to prepare $NiMn_2O_4$@NC and $NiCo_2O_4$@NC using $NiMn_2$-NA and $NiCo_2$-NA as the precursors, respectively. SEM and TEM measurements indicated that these samples presented nanowire morphologies assembled from MTMO@C nanoparticles (Figs. S6(a)–S6(c) and S7(a)–S7(c) in the ESM). The corresponding products were further confirmed using XRD (Figs. S6(d) and S7(d) in the ESM).

4 Conclusions

In summary, we demonstrated a facile and general strategy to synthesize binary transition metal oxide

nanoparticles (e.g., $MnCo_2O_4$, $NiMn_2O_4$, $NiCo_2O_4$) encapsulated in nitrogen-doped carbon. When employed as an electrocatalyst for water oxidation, $MnCo_2O_4$@NC had an outstanding electrocatalytic activity with low overpotential, a small Tafel slope, and high stability. The excellent performance was ensured by the synergistic effects between the $MnCo_2O_4$ and N-doped carbon, as well as the hierarchical structures of the hybrid. Moreover, a $MnCo_2O_4$@NC-based all-solid-state supercapacitor presented a high specific capacitance and an excellent cycling stability.

Acknowledgements

The project is supported by the National Basic Research Program of China (No. 2014CB660808), Jiangsu Provincial Founds for Distinguished Young Scholars (No. BK20130046), the National Natural Science Foundation of China (Nos. 61525402 and 21275076), QingLan Project, Program for New Century Excellent Talents in University (No. NCET-13-0853), Synergetic Innovation Center for Organic Electronics and Information Displays, the Priority Academic Program Development of Jiangsu Higher Education Institutions (PAPD), SERC Grant (No. 1021700142) from A*STAR, Singapore, the scholarship from China Scholarships Council (No. 201508320304), the Jiangsu Provincial Founds for Graduate Student Innovation Project (No. KYLX15_0821).

Electronic Supplementary Material: Supplementary material (FTIR spectrum, TGA measurements, EDX, etc.) is available in the online version of this article at http://dx.doi.org/10.1007/s12274-016-1025-x.

References

[1] Faber, M. S.; Jin, S. Earth-abundant inorganic electrocatalysts and their nanostructures for energy conversion applications. *Energy Environ. Sci.* **2014**, *7*, 3519–3542.

[2] Aricò, A. S.; Bruce, P.; Scrosati, B.; Tarascon, J.-M.; Van Schalkwijk, W. Nanostructured materials for advanced energy conversion and storage devices. *Nat. Mater.* **2005**, *4*, 366–377.

[3] Lewis, N. S.; Nocera, D. G. Powering the planet: Chemical challenges in solar energy utilization. *Proc. Natl. Acad. Sci. USA* **2006**, *103*, 15729–15735.

[4] Xia, W.; Mahmood, A.; Zou, R. Q.; Xu, Q. Metal–organic frameworks and their derived nanostructures for electrochemical energy storage and conversion. *Energy Environ. Sci.* **2015**, *8*, 1837–1866.

[5] Zhang, J. T.; Zhao, Z. H.; Xia, Z. H.; Dai, L. M. A metal-free bifunctional electrocatalyst for oxygen reduction and oxygen evolution reactions. *Nat. nanotechnol.* **2015**, *10*, 444–452.

[6] Kanan, M. W.; Nocera, D. G. *In situ* formation of an oxygen-evolving catalyst in neutral water containing phosphate and Co^{2+}. *Science* **2008**, *321*, 1072–1075.

[7] Fabbri, E.; Habereder, A.; Waltar, K.; Kötz, R.; Schmidt, T. J. Developments and perspectives of oxide-based catalysts for the oxygen evolution reaction. *Catal. Sci. Technol.* **2014**, *4*, 3800–3821.

[8] Lee, Y.; Suntivich, J.; May, K. J.; Perry, E. E.; Shao-Horn, Y. Synthesis and activities of rutile IrO_2 and RuO_2 nanoparticles for oxygen evolution in acid and alkaline solutions. *J. Phys. Chem. Lett.* **2012**, *3*, 399–404.

[9] Liu, Y. Y.; Wang, H. T.; Lin, D. C.; Liu, C.; Hsu, P.-C.; Liu, W.; Chen, W.; Cui, Y. Electrochemical tuning of olivine-type lithium transition-metal phosphates as efficient water oxidation catalysts. *Energy Environ. Sci.* **2015**, *8*, 1719–1724.

[10] Merki, D.; Hu, X. Recent developments of molybdenum and tungsten sulfides as hydrogen evolution catalysts. *Energy Environ. Sci.* **2011**, *4*, 3878–3888.

[11] Rosen, J.; Hutchings, G. S.; Jiao, F. Ordered mesoporous cobalt oxide as highly efficient oxygen evolution catalyst. *J. Am. Chem. Soc.* **2013**, *135*, 4516–4521.

[12] Wang, H. L.; Liang, Y. Y.; Gong, M.; Li, Y. G.; Chang, W.; Mefford, T.; Zhou, J. G.; Wang, J.; Regier, T.; Wei, F. J. An ultrafast nickel-iron battery from strongly coupled inorganic nanoparticle/nanocarbon hybrid materials. *Nat. Commun.* **2012**, *3*, 917.

[13] Yuan, C. Z.; Wu, H. B.; Xie, Y.; Lou, X. W. D. Mixed transition-metal oxides: Design, synthesis, and energy-related applications. *Angew. Chem., Int. Ed.* **2014**, *53*, 1488–1504.

[14] Zhang, Y. F.; Li, L. Q.; Su, H. Q.; Huang, W.; Dong, X. C. Binary metal oxide: Advanced energy storage materials in supercapacitors. *J. Mater. Chem. A* **2015**, *3*, 43–59.

[15] McCrory, C. C. L.; Jung, S.; Peters, J. C.; Jaramillo, T. F. Benchmarking heterogeneous electrocatalysts for the oxygen evolution reaction. *J. Am. Chem. Soc.* **2013**, *135*, 16977–16987.

[16] Zhou, R. F.; Jaroniec, M.; Qiao, S. Z. Nitrogen-doped carbon electrocatalysts decorated with transition metals for the oxygen reduction reaction. *ChemCatChem* **2015**, *7*, 3808–3817.

[17] Padmanathan, N.; Selladurai, S. Mesoporous $MnCo_2O_4$ spinel oxide nanostructure synthesized by solvothermal technique for supercapacitor. *Ionics* **2014**, *20*, 479–487.

[18] Liang, Y. Y.; Wang, H. L.; Diao, P.; Chang, W.; Hong, G. S.; Li, Y. G.; Gong, M.; Xie, L. M.; Zhou, J. G.; Wang, J. et al. Oxygen reduction electrocatalyst based on strongly coupled cobalt oxide nanocrystals and carbon nanotubes. *J. Am. Chem. Soc.* **2012**, *134*, 15849–15857.

[19] Liu, M. M.; He, S. J.; Chen, W. Co_3O_4 nanowires supported on 3D N-doped carbon foam as an electrochemical sensing platform for efficient H_2O_2 detection. *Nanoscale* **2014**, *6*, 11769–11776.

[20] Liang, Y. Y.; Li, Y. G.; Wang, H. L.; Zhou, J. G.; Wang, J.; Regier, T.; Dai, H. J. Co_3O_4 nanocrystals on graphene as a synergistic catalyst for oxygen reduction reaction. *Nat. Mater.* **2011**, *10*, 780–786.

[21] Zhang, P.; Sun, F.; Xiang, Z. H.; Shen, Z. G.; Yun, J.; Cao, D. P. ZIF-derived *in situ* nitrogen-doped porous carbons as efficient metal-free electrocatalysts for oxygen reduction reaction. *Energy Environ. Sci.* **2014**, *7*, 442–450.

[22] Wood, K. N.; O'Hayre, R.; Pylypenko, S. Recent progress on nitrogen/carbon structures designed for use in energy and sustainability applications. *Energy Environ. Sci.* **2014**, *7*, 1212–1249.

[23] Wang, X. W.; Sun, G. Z.; Routh, P.; Kim, D.-H.; Huang, W.; Chen, P. Heteroatom-doped graphene materials: Syntheses, properties and applications. *Chem. Soc. Rev.* **2014**, *43*, 7067–7098.

[24] Zhang, J.; Xia, Z.; Dai, L. Carbon-based electrocatalysts for advanced energy conversion and storage. *Sci. Adv.* **2015**, *1*, e1500564.

[25] Liu, M. M.; Zhang, R. Z.; Chen, W. Graphene-supported nanoelectrocatalysts for fuel cells: Synthesis, properties, and applications. *Chem. Rev.* **2014**, *114*, 5117–5160.

[26] Xia, B. Y.; Yan, Y.; Wang, X.; Lou, X. W. D. Recent progress on graphene-based hybrid electrocatalysts. *Mater. Horiz.* **2014**, *1*, 379–399.

[27] Chen, S.; Qiao, S.-Z. Hierarchically porous nitrogen-doped graphene–$NiCo_2O_4$ hybrid paper as an advanced electrocatalytic water-splitting material. *ACS Nano* **2013**, *7*, 10190–10196.

[28] Hou, Y.; Li, J. Y.; Wen, Z. H.; Cui, S. M.; Yuan, C.; Chen, J. H. Co_3O_4 nanoparticles embedded in nitrogen-doped porous carbon dodecahedrons with enhanced electrochemical properties for lithium storage and water splitting. *Nano Energy* **2015**, *12*, 1–8.

[29] Wang, Y.; Shi, Y. M.; Zhao, C. X.; Wong, J. I.; Sun, X. W.; Yang, H. Y. Printed all-solid flexible microsupercapacitors: Towards the general route for high energy storage devices. *Nanotechnology* **2014**, *25*, 094010.

[30] Sun, C. C.; Ma, M. Z.; Yang, J.; Zhang, Y. F.; Chen, P.; Huang, W.; Dong, X. C. Phase-controlled synthesis of α-NiS nanoparticles confined in carbon nanorods for high performance supercapacitors. *Sci. Rep.* **2014**, *4*, 7054.

[31] Ferrari, A. C.; Meyer, J. C.; Scardaci, V.; Casiraghi, C.; Lazzeri, M.; Mauri, F.; Piscanec, S.; Jiang, D.; Novoselov, K. S.; Roth, S. et al. Raman spectrum of graphene and graphene layers. *Phys. Rev. Lett.* **2006**, *97*, 187401.

[32] Li, Z. P.; Mi, Y. J.; Liu, X. H.; Liu, S.; Yang, S. R.; Wang, J. Q. Flexible graphene/MnO_2 composite papers for supercapacitor electrodes. *J. Mater. Chem.* **2011**, *21*, 14706–14711.

[33] Liang, Y. Y.; Wang, H. L.; Zhou, J. G.; Li, Y. G.; Wang, J.; Regier, T.; Dai, H. J. Covalent hybrid of spinel manganese–cobalt oxide and graphene as advanced oxygen reduction electrocatalysts. *J. Am. Chem. Soc.* **2012**, *134*, 3517–3523.

[34] Yang, Y.; Lun, Z. Y.; Xia, G. L.; Zheng, F. C.; He, M. N.; Chen, Q. W. Non-precious alloy encapsulated in nitrogen-doped graphene layers derived from MOFs as an active and durable hydrogen evolution reaction catalyst. *Energy Environ. Sci.* **2015**, *8*, 3563–3571.

[35] Sharifi, T.; Hu, G. Z.; Jia, X. E.; Wågberg, T. Formation of active sites for oxygen reduction reactions by transformation of nitrogen functionalities in nitrogen-doped carbon nanotubes. *ACS Nano* **2012**, *6*, 8904–8912.

[36] Zheng, F. C.; Yang, Y.; Chen, Q. W. High lithium anodic performance of highly nitrogen-doped porous carbon prepared from a metal–organic framework. *Nat. Commun.* **2014**, *5*, 5261.

[37] Zou, X. X.; Huang, X. X.; Goswami, A.; Silva, R.; Sathe, B. R.; Mikmeková, E.; Asefa, T. Cobalt-embedded nitrogen-rich carbon nanotubes efficiently catalyze hydrogen evolution reaction at all pH values. *Angew. Chem.* **2014**, *126*, 4461–4465.

[38] Silva, R.; Voiry, D.; Chhowalla, M.; Asefa, T. Efficient metal-free electrocatalysts for oxygen reduction: Polyaniline-derived N- and O-doped mesoporous carbons. *J. Am. Chem. Soc.* **2013**, *135*, 7823–7826.

[39] Li, H. H.; Xu, R. Y.; Wang, Y. P.; Qian, B. B.; Wang, H. B.; Chen, L.; Jiang, H. B.; Yang, Y. L.; Xu, Y. Y. *In situ* synthesis of hierarchical mesoporous Fe_3O_4@C nanowires derived from coordination polymers for high-performance lithium-ion batteries. *RSC Adv.* **2014**, *4*, 51960–51965.

[40] Ren, J. W.; Antonietti, M.; Fellinger, T. P. Efficient water splitting using a simple Ni/N/C paper electrocatalyst. *Adv. Energy Mater.* **2015**, *5*, 1401660.

[41] Song, H. W.; Li, N.; Cui, H.; Wen, X.; Wei, X. L.; Wang, C. X. Significantly improved high-rate Li-ion batteries anode by encapsulating tin dioxide nanocrystals into mesotunnels. *CrystEngComm* **2013**, *15*, 8537–8543.

[42] Li, N.; Song, H. W.; Cui, H.; Yang, G. W.; Wang, C. X. Self-assembled growth of Sn@CNTs on vertically aligned graphene for binder-free high Li-storage and excellent stability. *J. Mater. Chem. A* **2014**, *2*, 2526–2537.

[43] Han, Y. Z.; Tang, D.; Yang, Y. M.; Li, C. X.; Kong, W. Q.; Huang, H.; Liu, Y.; Kang, Z. H. Non-metal single/dual doped carbon quantum dots: A general flame synthetic method and electro-catalytic properties. *Nanoscale* **2015**, *7*, 5955–5962.

[44] Wang, B.; Zhu, T.; Wu, H. B.; Xu, R.; Chen, J. S.; Lou, X. W. D. Porous Co_3O_4 nanowires derived from long $Co(CO_3)_{0.5}(OH)\cdot 0.11H_2O$ nanowires with improved supercapacitive properties. *Nanoscale* **2012**, *4*, 2145–2149.

[45] Kong, D. Z.; Cheng, C. W.; Wang, Y.; Wong, J. I.; Yang, Y. P.; Yang, H. Y. Three-dimensional Co_3O_4@C@Ni_3S_2 sandwich-structured nanoneedle arrays: Towards high-performance flexible all-solid-state asymmetric supercapacitors. *J. Mater. Chem. A* **2015**, *3*, 16150–16161.

[46] Wang, Q. F.; Xu, J.; Wang, X. F.; Liu, B.; Hou, X. J.; Yu, G.; Wang, P.; Chen, D.; Shen, G. Z. Core–shell $CuCo_2O_4$@MnO_2 nanowires on carbon fabrics as high-performance materials for flexible, all-solid-state, electrochemical capacitors. *ChemElectroChem* **2014**, *1*, 559–564.

[47] He, Y. M.; Chen, W. J.; Li, X. D.; Zhang, Z. X.; Fu, J. C.; Zhao, C. H.; Xie, E. Q. Freestanding three-dimensional graphene/MnO_2 composite networks as ultralight and flexible supercapacitor electrodes. *ACS Nano* **2013**, *7*, 174–182.

[48] Yuan, L. Y.; Lu, X.-H.; Xiao, X.; Zhai, T.; Dai, J. J.; Zhang, F. C.; Hu, B.; Wang, X.; Gong, L.; Chen, J. et al. Flexible solid-state supercapacitors based on carbon nanoparticles/MnO_2 nanorods hybrid structure. *Acs Nano* **2012**, *6*, 656–661.

[49] Liao, Q. Y.; Li, N.; Jin, S. X.; Yang, G. W.; Wang, C. X. All-solid-state symmetric supercapacitor based on Co_3O_4 nanoparticles on vertically aligned graphene. *ACS Nano* **2015**, *9*, 5310–5317.

[50] Xu, Y. X.; Wu, Q.; Sun, Y. Q.; Bai, H.; Shi, G. Q. Three-dimensional self-assembly of graphene oxide and DNA into multifunctional hydrogels. *ACS Nano* **2010**, *4*, 7358–7362.

[51] Wu, Z. S.; Winter, A.; Chen, L.; Sun, Y.; Turchanin, A.; Feng, X. L.; Müllen, K. Three-dimensional nitrogen and boron co-doped graphene for high-performance all-solid-state supercapacitors. *Adv. Mater.* **2012**, *24*, 5130–5135.

[52] Song, H. W.; Shen, L. S.; Wang, C. X. Template-free method towards quadrate Co_3O_4 nanoboxes from cobalt coordination polymer nano-solids for high performance lithium ion battery anodes. *J. Mater. Chem. A* **2014**, *2*, 20597–20604.

[53] Yang, G. Z.; Cui, H.; Yang, G. W.; Wang, C. X. Self-assembly of $Co_3V_2O_8$ multilayered nanosheets: Controllable synthesis, excellent Li-storage properties, and investigation of electrochemical mechanism. *ACS Nano* **2014**, *8*, 4474–4487.